ACS NANO
Cite This: ACS Nano 2019, 13, 408–420
www.acsnano.org

ARTICLE

Multifunctional Self-Assembled Supernanoparticles for Deep-Tissue Bimodal Imaging and Amplified Dual-Mode Heating Treatment

Fan Yang,[†] Artiom Skripka,[†] Maryam Sadat Tabatabaei,[‡] Sung Hwa Hong,[∥] Fuqiang Ren,[†] Antonio Benayas,[†,§] Jung Kwon Oh,[∥] Sylvain Martel,[‡] Xinyu Liu,[⊥] Fiorenzo Vetrone,*[,†] and Dongling Ma*[,†]

[†]Institut National de la Recherche Scientifique, Centre Énergie, Matériaux et Télécommunications, Université du Québec, 1650 Boulevard Lionel-Boulet, Varennes, Quebec J3X 1S2, Canada

[‡]NanoRobotics Laboratory, Department of Computer and Software Engineering, Institute of Biomedical Engineering, Polytechnique Montréal, Montreal, Quebec H3T 1J4, Canada

[∥]Department of Chemistry and Biochemistry, Concordia University, Montreal, Quebec H4B 1R6, Canada

[§]Department of Physics and CICECO−Aveiro Institute of Materials, University of Aveiro, 3810-193, Aveiro, Portugal

[⊥]Department of Mechanical and Industrial Engineering, University of Toronto, 5 King's College Road, Toronto, Ontario M5S 3G8, Canada

Supporting Information

ABSTRACT: **Developing multifunctional therapeutic and diagnostic (theranostic) nanoplatforms is critical for addressing challenging issues associated with cancers. Here, self-assembled supernanoparticles consisting of superparamagnetic Fe_3O_4 nanoparticles and photoluminescent PbS/CdS quantum dots whose emission lies within the second biological window (II-BW) are developed. The proposed self-assembled Fe_3O_4 and PbS/CdS (II-BW) supernanoparticles [SASNs (II-BW)] exhibit outstanding photoluminescence detectable through a tissue as thick as 14 mm, by overcoming severe light extinction and concomitant autofluorescence in II-BW, and significantly enhanced T_2 relaxivity (282 mM^{-1} s^{-1}, *ca.* 4 times higher than free Fe_3O_4 nanoparticles) due to largely enhanced magnetic field inhomogeneity. On the other hand, SASNs (II-BW) possess the dual capacity to act as both magnetothermal and photothermal agents, overcoming the main drawbacks of each type of heating separately. When SASNs (II-BW) are exposed to the dual-mode (magnetothermal and photothermal) heating, the thermal energy transfer efficiency is amplified 7-fold compared with magnetic heating alone. These results, in hand with the excellent photo- and colloidal stability, and negligible cytotoxicity, demonstrate the potential use of SASNs (II-BW) for deep-tissue bimodal (magnetic resonance and photoluminescence) *in vivo* imaging, while simultaneously providing the possibility of SASNs (II-BW)-mediated amplified dual-mode heating treatment for cancer therapy.**

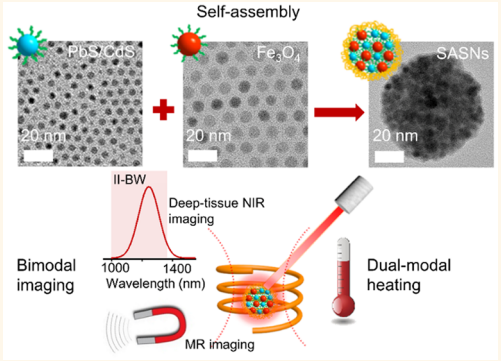

KEYWORDS: *self-assembly, multifunctional supernanoparticles, second biological window, bimodal imaging, dual-modal heating*

Emerging nanotechnologies have driven the development of multifunctional (superparamagnetic and photoluminescent) nanoparticles (NPs) to fulfill the increasing needs of contrast agents suited for a bimodal [magnetic resonance (MR) and photoluminescence] imaging approach.[1−3] Various bimodal contrast agents have been fabricated, including dye-incorporated iron oxide nanocomposites, hybrid nanomaterials composed of magnetic NPs and upconversion nanoparticles, magnetically doped quantum dots (QDs), and clusters of Fe_3O_4 NPs and visible QDs.[2−4] Nevertheless, the photoluminescent component of these NPs in most studies operates within the visible range, which results in shallow penetration depth and ambiguous photolumines-

Received: August 28, 2018
Accepted: December 31, 2018
Published: January 3, 2019

DOI: 10.1021/acsnano.8b06563
ACS Nano 2019, 13, 408−420

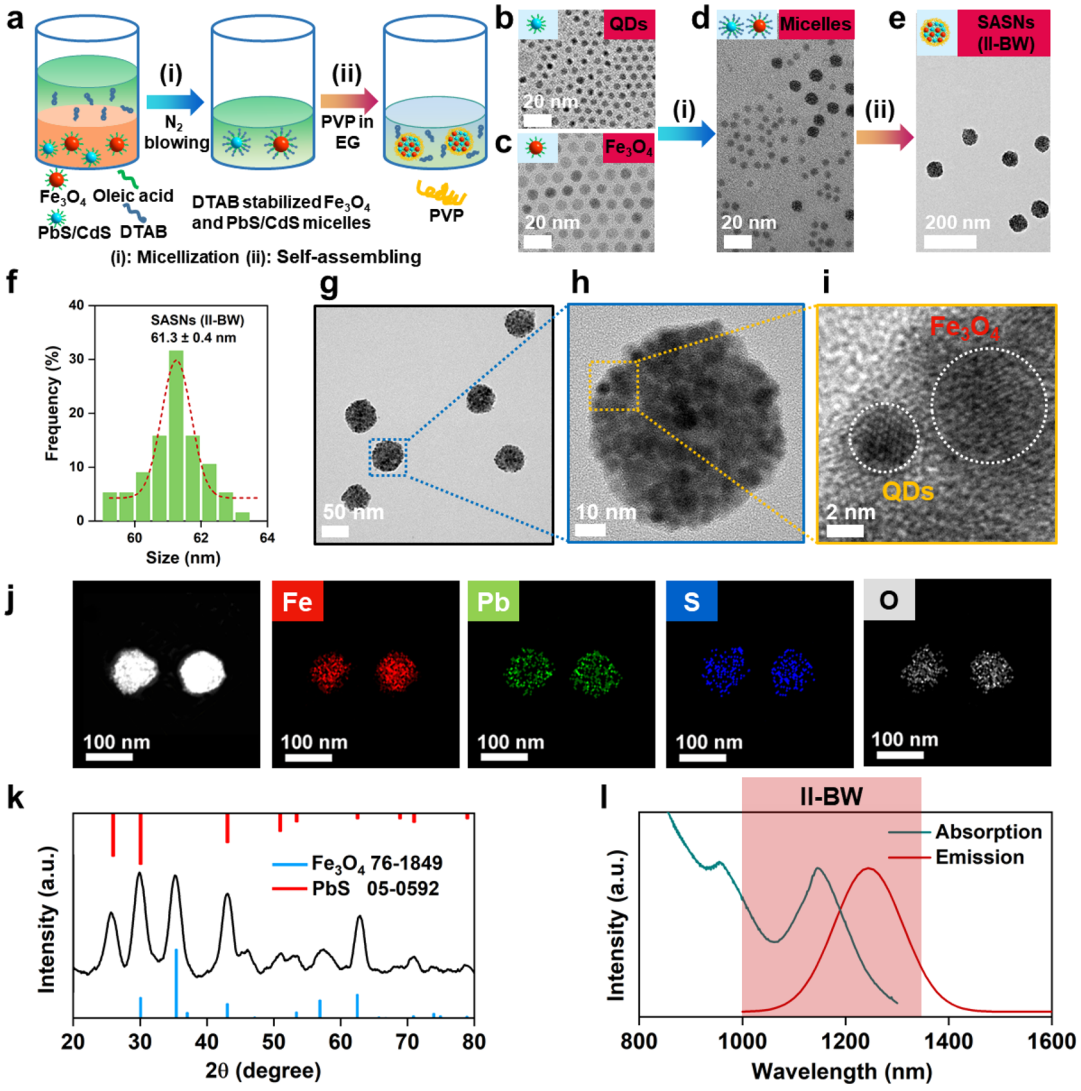

Figure 1. (a) Schematic illustration of the formation process of SASNs (II-BW). (b, c) TEM images of PbS/CdS (II-BW) QDs and Fe_3O_4 dispersed in chloroform. (d) DTAB-stabilized PbS/CdS (II-BW) and Fe_3O_4 micelles. (e) SASNs (II-BW). (f) Size distribution of SASNs (II-BW). (g–i) TEM images of SASNs (II-BW) at different magnifications. (j) HAADF-STEM image and EDX-elemental maps of SASNs (II-BW). (k) XRD pattern of SASNs (II-BW). Standard peaks of Fe_3O_4 (blue, JCPDS 76-1849) and PbS (red, JCPDS 05-0592) are shown. (l) Absorption and photoluminescence emission spectra of SASNs (II-BW).

cence signals due to the tissue-induced light extinction and autofluorescence, thus limiting their use as deep-tissue *in vivo* photoluminescence probes.[5] By introducing NPs with absorption and emission wavelengths in the biological windows (BW) located in the near-infrared (NIR) range (I-BW: 700−950 nm; II-BW: 1000−1350 nm),[6−8] these challenges can be overcome, enabling deep-tissue photoluminescent imaging with high signal-to-noise ratio. Biological tissues in BWs are considered to be optically transparent because the optical extinction (absorption and scattering) of NIR photons can be largely avoided and the autofluorescence background greatly diminished.[5,9−11] Thus, it is substantially beneficial to engineer new multifunctional (superparamagnetic and photoluminescent) NPs, employing NIR-modulated probes for deep-tissue *in vivo* bimodal imaging. Recently Dai *et al.* reported a bright non-toxic photoluminescence probe based on PbS/CdS (II-BW) QDs, which allows for non-invasive deep-tissue photoluminescence imaging with high spatial resolution in 2D/3D confocal modes and real-time photoluminescence imaging of vascular regeneration with dynamic tissue perfusion.[12,13] Also, our group has worked on a series of Pb-based QDs such as PbS, PbS/CdS, and PbS/CdS/ZnS, which exhibit excellent NIR photoluminescence properties.[14−22] However, research regarding hybrid bimodal contrast agents, which combine Fe_3O_4 NPs and promising Pb-based NIR QDs, has not been reported thus far.

Magnetothermal therapy is a well-known thermal cancer treatment technique in which heat is induced by Néel and Brownian relaxation of magnetic NPs when exposed to an alternating magnetic field (AMF).[23] Jordan *et al.* reported the first clinical application of magnetothermal therapy in locally recurrent prostate cancer in 2005.[24] Subsequently, a variety of clinical trials were carried out worldwide,[25,26] paving the way for NanoTherm Therapy (MagForce AG) in commercial clinical settings.[27] Similarly, photothermal therapy employing NIR light absorbing agents to generate heat from NIR laser irradiation to burn cancer cells has received considerable attention because of its advantages including non-invasiveness, high specificity, and precise spatiotemporal selectivity.[28−31] In addition, our previous collaborative work demonstrated Pb-

DOI: 10.1021/acsnano.8b06563
ACS Nano 2019, 13, 408−420

based NIR QDs can act as efficient temperature self-monitored photothermal agents.[32]

There are still drawbacks that must be addressed in both magnetothermal and photothermal therapeutics. For example, magnetothermal therapy agents are used at quite high concentrations ([Fe] = 1−2 M, several orders of magnitude higher than the concentration used for MR imaging), which remains a strong concern in the clinical setting. Because of the relatively poor thermal energy transfer efficiency of magnetic NPs [defined as specific loss power (SLP), the power dissipation per unit of mass of the magnetic material], large amounts are required to efficiently convert magnetic energy into heat.[33] For diagnostic purposes, such high concentration cannot be used for MR imaging because of the signal void in the areas containing high concentrations of magnetic NPs.[34] On the other hand, photothermal therapy is not applicable to malignancies in distant organs due to the limited penetration depth of NIR light into the tissue.[28] In this regard, magnetothermal therapy can ignore problems associated with light tissue penetration as radiofrequency electromagnetic waves are exploited for the magnetic heating.[33] Given these issues, integrating magnetothermal and photothermal therapy into a single nanoplatform may provide a dual-mode therapeutic approach to realize high-efficiency and deep-tissue cancer treatment. Claire *et al.* have demonstrated that the simultaneous stimulation of iron oxide nanocubes under both AMF and NIR laser irradiation offers remarkable heating efficiency, addressing the individual challenges of any monomagnetic and mono-optical heating modality for iron oxide.[35] Although overwhelming heating can be achieved by this nanoplatform, their biomedical applications are restricted due to lack of appropriate diagnostic modality.

Self-assembled supernanoparticles (SASNs) can be regarded as the collections of individual colloidal NPs by self-assembly, which allow for the rational control of the optical, plasmonic, electronic, and/or magnetic phenomena pairing between distinct NPs. In this way, supernanoparticles (SNs) possess not only the intrinsic physical and chemical characteristics of their individual NPs but also the collective properties of these NPs due to coupling effects.[36] For example, self-assembled binary magnetic superlattice membranes exhibit collective interparticle dipolar interactions,[37] and iron oxide clusters cause remarkably enhanced T_2 relaxivity in MR imaging.[38] Notably, the self-assembly approach is a simple, reproducible, and inexpensive way to synthesize multifunctional SNs by combing two or more types of independently tailored NPs. For instance, Bawendi *et al.* demonstrated the preparation of magneto-photoluminescent SNs based on coassembling CdSe/CdS QDs and Fe_3O_4 NPs and their application for *in vivo* bimodal imaging of mice bearing murine mammary carcinoma.[39]

Here, we present multifunctional self-assembled Fe_3O_4 and PbS/CdS (II-BW) supernanoparticles [SASNs (II-BW)] aimed at synergistic bimodal imaging and heating treatment, based on their outstanding superparamagnetic and NIR photoluminescence properties. Our *ex vivo* deep-tissue imaging experiments revealed that the NIR emission, lying within II-BW, endows the SASNs (II-BW) with deep-tissue penetrating capabilities beneficial for optical bioimaging, superior to their counterpart operating within I-BW [SASNs (I-BW)]. Meanwhile, owing to the synergistic effect of their clustering characteristic, SASNs (II-BW) exhibit a significantly enhanced T_2 relaxivity for MR imaging compared with that of free Fe_3O_4 NPs. In addition, the SASNs (II-BW) allow us to perform photoluminescence tracking by magnetic confinement, enabling potential application for high-sensitivity detection of cancer cells. Subsequently, we demonstrate that SASNs (II-BW) can be stimulated by dual-mode heating, which provides an unrivaled SLP, overcoming the main drawbacks of magnetothermal or photothermal therapy individually. The multifunctional SASNs (II-BW) developed here could be suitable not only for deep-tissue bimodal imaging but also for dual-mode heating treatment, rendering them an excellent candidate for realizing future multipronged cancer theranostics.

RESULTS AND DISCUSSION

Schematics of the self-assembling procedures for preparing superparamagnetic and photoluminescent SASNs (II-BW) are shown in Figure 1a. Core/shell PbS/CdS QDs (Figure 1b and Figure S1b) synthesized by microwave-assisted cation exchange of PbS QDs (Figure S1a), with their emission band at *ca.* 1260 nm (II-BW) (Figure S2), were chosen as the photoluminescent component.[40] The average diameter of PbS/CdS QDs was about 4.7 ± 0.3 nm (Figure S3). Meanwhile, high-quality Fe_3O_4 NPs (Figure 1c) with an average size about 8.3 ± 0.7 nm in diameter (Figure S3) were used as the superparamagnetic part. In the first step, by using dodecyltrimethylammonium bromide (DTAB) as a surfactant, oleic acid capped PbS/CdS QDs and Fe_3O_4 NPs dispersed in chloroform were transferred into water by micellar encapsulation, due to hydrophobic van der Waals interactions between the hydrocarbon chains of oleic acid and DTAB. After water transfer, it can be observed that the PbS/CdS and Fe_3O_4 NPs trapped in the micelles retain their monodispersity and size (Figure 1d). In the second step, the aqueous dispersion of PbS/CdS and Fe_3O_4 micelles was quickly injected into the ethylene glycol (EG) solution of polyvinylpyrrolidone (PVP), in which the van der Waals interactions between oleic acid ligands and DTAB surfactants were gradually weakened.[41] This resulted in the loss of DTAB molecules from the PbS/CdS QDs and Fe_3O_4 NPs, engulfing micelles, and eventually led to the decomposition of these micelles. As a consequence, the self-assembling process occurred, aggregating the PbS/CdS QDs and Fe_3O_4 NPs, owing to the introduced solvophobic interaction between the oleic acid ligands on the surface of NPs and the EG solution. Meanwhile, PVP acted as a capping agent, coating the SASNs (II-BW) and stabilizing them against further aggregation of individual SNs through repulsive steric interactions.[42] The principal infrared vibrations of C═O, C−N, and CH_2 functional groups in the Fourier-transform infrared (FTIR) spectrum (Figure S4) confirm the PVP capping on the SASNs (II-BW). The resulting 3D spherical SASNs (II-BW) with an average size of 61.3 ± 0.4 nm in diameter (Figure 1f) are shown in Figure 1e.

In order to verify the morphology and distribution of the Fe_3O_4 NPs and PbS/CdS QDs inside the SASNs (II-BW), transmission electron microscopy (TEM) images at different magnifications, high-angle annular dark-field scanning transmission electron microscopy (HAADF-STEM), and energy dispersive X-ray (EDX)-elemental mapping were acquired (Figure 1g−j). The higher magnification TEM images demonstrate that each SASN (II-BW) is composed of multiple randomly distributed Fe_3O_4 NPs and PbS/CdS QDs. The molar ratio of Fe/Pb was found to be 1:1.2 as measured by inductively coupled plasma-optical emission spectrometry (ICP-OES), which is in agreement with the initially employed

DOI: 10.1021/acsnano.8b06563
ACS Nano 2019, 13, 408−420

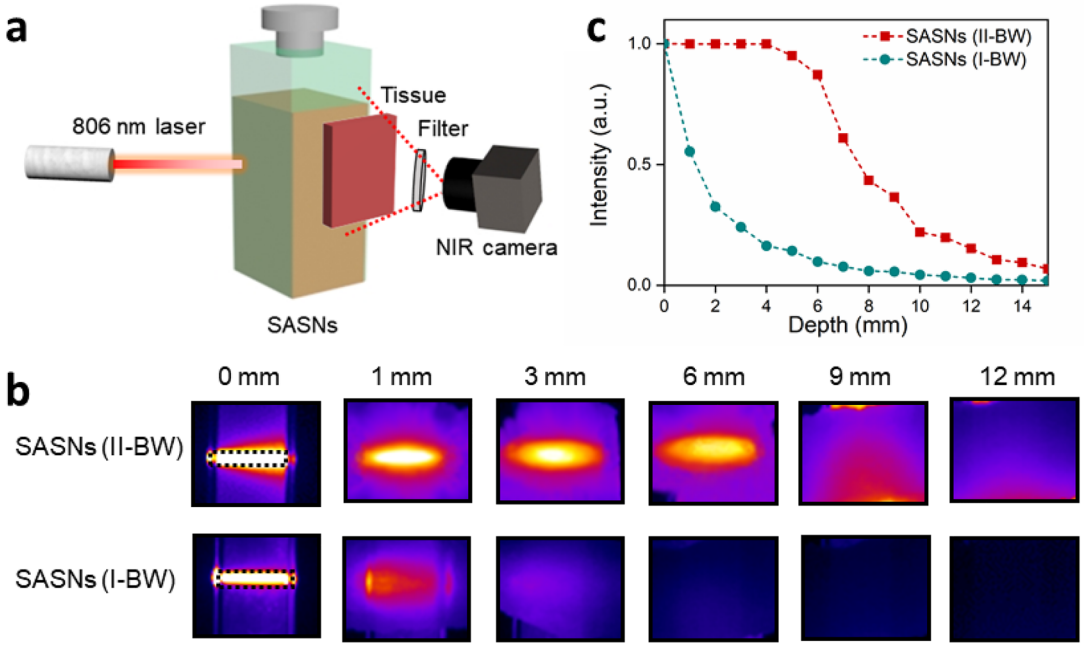

Figure 2. (a) Scheme of the experiment setup for demonstrating *ex vivo* NIR imaging through pork tissue of various thicknesses, placed on one side of the cuvette filled with an aqueous solution containing SASNs. (b) *Ex vivo* NIR images through pork tissue of different thicknesses (0, 1, 3, 6, 9, and 12 mm) for SASNs (I-BW) and SASNs (II-BW) under 806 nm laser excitation. The power density of the 806 nm laser was adjusted to 10 W/cm^2 in both cases. (c) Normalized emission intensity of SASNs (I-BW) and SASNs (II-BW) as a function of penetration depth in pork tissue. Emitted intensity was calculated from the region of interest denoted by a dashed black rectangle.

ratio of Fe_3O_4 NPs and PbS/CdS QDs. Meanwhile, this ratio is anticipated to be an optimal value for photoluminescent imaging (Figure S5). Owing to their different sizes (Figure S2), it is easy to distinguish the Fe_3O_4 NPs and PbS/CdS QDs (Figure 1h,i). Through the corresponding HAADF-STEM and EDX-elemental maps, it can be observed that Fe, Pb, S, and O elements are homogeneously distributed over the entire SASNs' volume. In addition, the X-ray diffraction (XRD) pattern (Figure 1k) verifies the coexistence of Fe_3O_4 NPs and PbS/CdS QDs in the SASNs (II-BW). Figure 1l shows the absorption and emission spectra of SASNs (II-BW). The first-order excitonic absorption and emission bands of SASNs (II-BW) are located at around 1150 and 1240 nm, respectively, covering most of the II-BW's spectral range. Interestingly, compared with the bare PbS/CdS (II-BW) QDs (absorption: 1185 nm, emission: 1260 nm) (Figure S1), the absorption and emission peaks of SASNs (II-BW) show a blue shift, which can be attributed to the change of electronic density in the surface states of immobilized QDs under passivation by the PVP coating.[43,44]

In the meantime, we have adopted the same self-assembling protocol to prepare similar superparamagnetic and photoluminescent SASNs (I-BW) by using smaller PbS/CdS (I-BW) QDs (Figure S6a) with an average size about 2.9 ± 0.3 nm in diameter (Figure S6b) and possessing an emission band centered at *ca.* 915 nm (Figure S6c). The same Fe_3O_4 NPs (Figure 1c) were employed as the superparamagnetic component to prepare SASNs (I-BW). After self-assembling with Fe_3O_4 NPs, the prepared SASNs (I-BW) (Figure S7a) show similar morphology to previously observed SASNs (II-BW) and have an average size about 59.7 ± 0.9 nm (Figure S7b). Due to the larger size difference between the Fe_3O_4 and smaller PbS/CdS (I-BW) QDs with respect to the PbS/CdS (II-BW) QDs, it is easier to identify the Fe_3O_4 and PbS/CdS QDs in the SASNs (I-BW). After self-assembly, the absorption and emission peaks of SASNs (I-BW) show a slight blue shift (Figure S7c), which can be easily understood following the same reasoning as in the case of SASNs (II-BW).

In order to assess and compare the deep-tissue bioimaging capabilities of SASNs (I-BW) and SASNs (II-BW), we have implemented an experimental setup (Figure 2a) in which pork tissue of different thickness was placed on one side of the cuvette filled with an aqueous solution containing the SASNs. Subsequently, NIR images were acquired by an NIR camera placed above the pork tissue. It is worth mentioning that the pork tissue herein was chosen to mimic human soft tissue, since it is photophysically closest to human soft tissue among commonly used animal tissue models.[45] Excitation of the SASNs was achieved by an 806 nm laser diode, which has been shown to be particularly well suited for optical bioimaging.[46,47] Foremost, NIR excitation at wavelengths such as 806 nm is superior to those on the visible spectral side due to the lower photo-induced cytotoxicity.[48] Moreover, the water absorption of 806 nm is significantly reduced compared to that of 980 nm (another commonly used wavelength for exciting NIR optical probes), which helps to reduce the undesired overheating effect of biological tissues. Here, the power density of the 806 nm laser (10 W/cm^2) spot on target and the concentration of both types of SASNs (0.8 mg/mL) were identical in both cases, to fairly compare the penetration depth of the photoluminescence signal from the SASNs (I-BW) and SASNs (II-BW). Figure 2b shows *ex vivo* NIR images through pork tissue with different thickness (0, 1, 3, 6, 9, and 12 mm) for SASNs (I-BW) and SASNs (II-BW). The corresponding collected light intensity, calculated from the region of interest (and normalized to 1.0 at 0 mm), as a function of pork tissue thickness is plotted in Figure 2c. We observed that SASNs (II-BW) showed a strong photoluminescence signal in the NIR

DOI: 10.1021/acsnano.8b06563
ACS Nano 2019, 13, 408−420

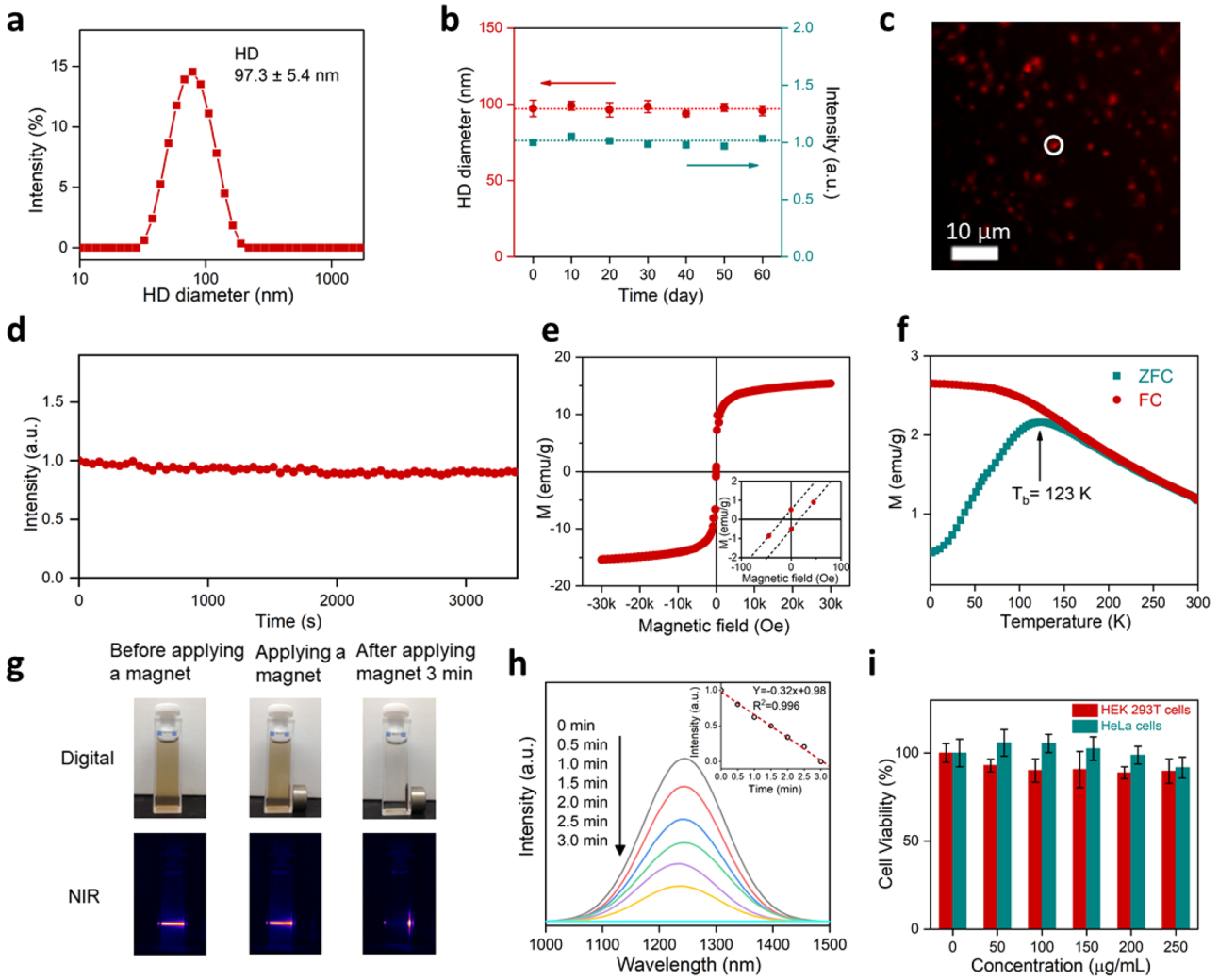

Figure 3. (a) Hydrodynamic diameter, denoted as HD, of the SASNs (II-BW). (b) Hydrodynamic diameter and normalized photoluminescence emission intensity of the SASNs (II-BW) as a function of storage time. (c) Photoluminescence imaging of the SASNs (II-BW) on a coverslip. (d) Photoluminescence intensity change with time for a single aggregate of SASNs (II-BW) denoted in (c). (e) Magnetization of SASNs (II-BW) as a function of magnetic field at 300 K. The inset shows the magnified view of the magnetization curve under low magnetic field. (f) Temperature-dependent ZFC and FC magnetization curves at 100 Oe for SASNs (II-BW). (g) Digital and NIR photographs of SASNs (II-BW) in aqueous solution before applying a magnet (left), applying a magnet (middle) at 0 min, and after applying the magnet for 3 min (right). The NIR images were taken by a NIR camera upon excitation of the SASNs (II-BW) with an 806 nm laser. (h) Photoluminescence emission spectra of the supernatant in SASNs (II-BW) solution measured every 30 s after applying a magnet shown in the middle of (g). The insert in (h) shows corresponding integrated intensity of supernatant (d) as a function of time. (i) Cytotoxicity study of SASNs (II-BW) on HeLa and HEK 293T cells cultured with various concentrations of SASNs (II-BW).

images and their emission intensity saturated the detector of the NIR camera for the ≤4 mm thick pork tissue; most importantly, the NIR signal could still be detected even when the pork tissue thickness reached 14 mm. However, regarding the SASNs (I-BW), the photoluminescence signal rapidly diminished with the increasing thickness of the pork tissue and dropped to ≤20% of the initial intensity by the 4 mm mark. These results indicate that the capability of deep-tissue penetration of SASNs (II-BW) is superior to that of SASNs (I-BW), since the optical extinction of tissue in the II-BW is reduced compared to that in the I-BWs, which is also in a good agreement with our previous report.[17] Therefore, the SASNs (II-BW) are expected to be better imaging probes for deep-tissue imaging, as their NIR emission is guaranteed to penetrate further in biological tissues. In the following text, we focus on studying the greater optical property of SASNs (II-BW) and further exploiting them for MR imaging and magnetothermal and photothermal experiments.

When NPs circulate in biological media such as blood, colloidal stability is a key parameter entangled with their physicochemical properties and strongly influences the NPs' interaction with biological media.[49] In order to better investigate the colloidal stability of SASNs (II-BW), long-term average size distribution as a criterion for evaluating colloidal stability was carried out by dynamic light scattering (DLS) measurements. The hydrodynamic diameter of SASNs (II-BW) was found to be 97.3 ± 5.4 nm (Figure 3a), and, most importantly, it was retained through a 60-day period (Figure 3b), revealing the superior colloidal stability of SASNs (II-BW). Alternatively, we also monitored the colloidal stability of SASNs (II-BW) by tracking their photoluminescence intensity against storage time (Figure 3b). No significant changes were observed throughout the 60-day period, once again confirming

DOI: 10.1021/acsnano.8b06563
ACS Nano 2019, 13, 408−420

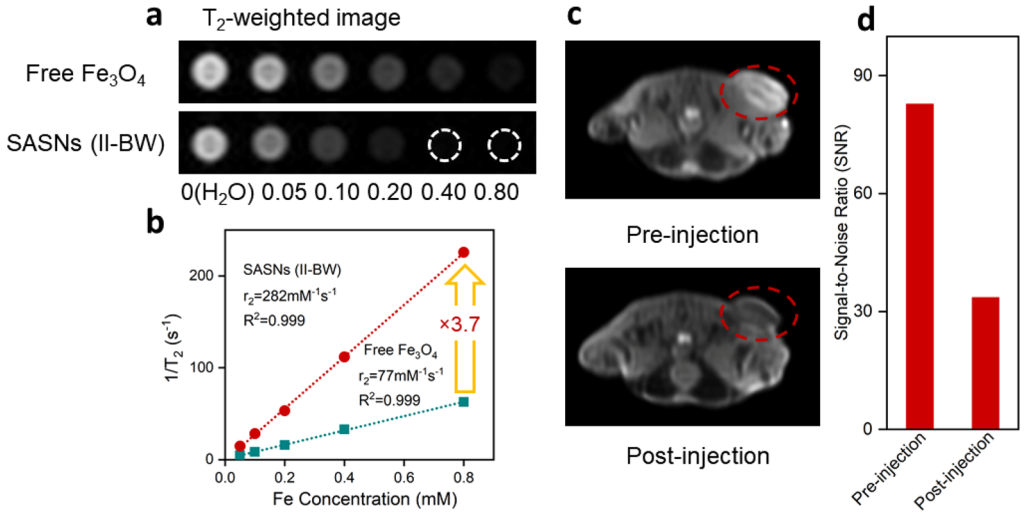

Figure 4. (a) T_2-weighted MR images of various Fe concentrations of SASNs (II-BW) and free Fe_3O_4 NPs, respectively. (b) Relaxation rate r_2 ($1/T_2$) *vs* different Fe concentrations of SASNs (II-BW) and free Fe_3O_4 NPs. (c) *In vivo* T_2-weighted MR images of a nude mouse bearing a tumor with transverse section taken at pre-injection and at 12 h intravenous post-injection of SASNs (II-BW). The position of the tumor is marked by a red dashed circle in (c). (d) Corresponding SNR in the tumor (c) at pre-injection and 12 h post-injection of the SASNs (II-BW).

the excellent colloidal stability of the developed SASNs. We attribute the long-term colloidal stability mainly to the PVP coating, which endows the SASNs (II-BW) with remarkable dispersibility in an aqueous milieu. It also shields the Fe_3O_4 NPs and PbS/CdS QDs from direct contact with water molecules, avoiding the quenching of PbS/CdS QDs with time. To testify whether SASNs (II-BW) show any photoluminescence photobleaching, SASNs (II-BW) were adsorbed and immobilized on a coverslip and imaged by a custom-built multiphoton hyperspectral microscope (Figure 3c). The plot of the photoluminescence intensity against time of a singled-out aggregate of multiple SASNs (II-BW) is shown in Figure 3d. Under illumination by an 808 nm laser for 3600 s, no evidence of photobleaching of the SASNs (II-BW) was observed, suggesting that SASNs (II-BW) possess remarkable photostability for deep-tissue photoluminescence imaging.

The magnetic properties of SASNs (II-BW) were characterized by field-dependent magnetization measurements, as shown in Figure 3e. The magnetization curve of SASNs (II-BW) shows the characteristic superparamagnetic behavior (near-zero coercivity and remanence) with a saturation magnetization of 15.4 emu/g at 300 K. This value is lower than that of free Fe_3O_4 (61.5 emu/g) (Figure S8) since the presence of the non-magnetic component of PbS/CdS (II-BW) QDs inside the SASNs (II-BW) reduces the relative mass ratio of the magnetic component, thus decreasing the value of the saturation magnetization per gram of SASNs (II-BW). The temperature-dependent zero-field-cooled (ZFC) and field-cooled (FC) magnetization measurements were performed under an applied field of 100 Oe between 5 and 300 K (Figure 3f). The ZFC and FC curves coincide at relatively high temperature but separate gradually with decreasing temperature since different sized particles in the same sample progressively block with decreasing temperature, which is a characteristic behavior of superparamagnetism.[50,51] The blocking temperature (T_b) is ~123 K, significantly lower than room temperature, suggesting the superparamagnetic properties of SASNs (II-BW) at room temperature. Furthermore, a relatively small external magnetic field was used to check whether the superparamagnetism of the SASNs (II-BW) can fulfill the requirement of easy and fast manipulation for future biomedical application (Figure 3g). From the digital images, it can be observed that the SASNs (II-BW) are well dispersed in solution prior to complete confinement by an externally placed magnet within about 3 min. Since the movement of the SASNs (II-BW) can be easily tracked by their photoluminescence, the NIR images of SASNs (II-BW) were acquired by a NIR camera under excitation of an 806 nm laser, further confirming the observed superparamagnetism and its effect on the rapid SASNs' confinement to the desired area. NIR images clearly show that the SASNs (II-BW) are sensitive to the magnetic field and can quickly accumulate in the direction of the applied magnetic field. It should be pointed out that the photoluminescence signal was only detected in the confined area under the magnetic field, indicating no free SASNs (II-BW), at a detectable level, were dispersed in the solution. In addition, the photoluminescence spectra of the supernatant in the SASNs (II-BW) solution were measured every 30 s with the applied external magnetic field (Figure 3h). The photoluminescence emission intensity decreased gradually with time, reaching almost zero by 3 min, which can be easily seen from the integrated emission intensity against time (inset of Figure 3h). This trend was consistent with the phenomenon observed in the NIR images, which indicates the rapid response of SASNs (II-BW) to the magnetic field. Interestingly, the integrated photoluminescence emission intensity shows a linear behavior, suggesting the homogeneous confinement of the SASNs (II-BW).

The cytotoxicity of SASNs (II-BW) at different concentrations was evaluated on HeLa cervical cancer cells and human embryonic kidney (HEK 293T) cells by the MTT assay (Figure 3i). Both HeLa cancer cells and HEK 293T cells showed no obvious toxicity (>90% cell viability), even at a significantly high concentration of 250 μg/mL, indicating the non-toxicity and good biocompatibility of SASNs (II-BW). The non-toxicity of SASNs (II-BW) mainly stems from the presence of the PVP coating, which effectively prevents the heavy metals (Pb and Cd) of the QDs from direct exposure to

DOI: 10.1021/acsnano.8b06563
ACS Nano 2019, 13, 408−420

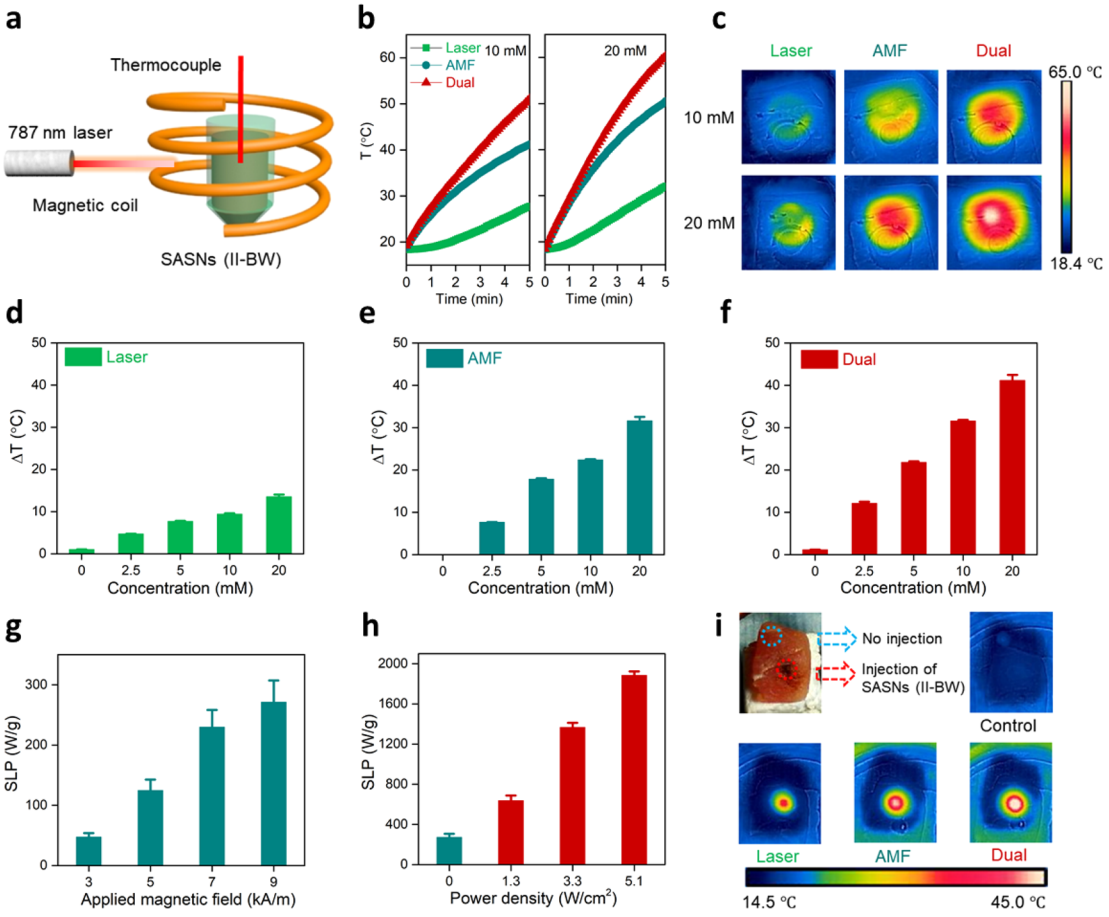

Figure 5. (a) Scheme of the setup for the combined magnetothermal and photothermal experiments. (b) Time-dependent temperature curves of solutions containing SASNs (II-BW) of 10 and 20 mM concentration under three types of modulation (laser at 3.3 W/cm^2, AMF at 7 kA/m, dual-mode). (c) Corresponding thermal images of SASNs (II-BW) solution after 5 min of each modulation. Thermal images are taken from the top of the tube with a cross-sectional view. Temperature increase of SASNs (II-BW) solutions at different concentrations after 5 min of each modulation: (d) laser at 3.3 W/cm^2, (e) AMF at 7 kA/m, and (f) dual-mode heating (laser at 3.3 W/cm^2 and AMF at 7 kA/m). SLP value of SASNs (II-BW) as a function of applied magnetic field (3, 5, 7, and 9 kA/m) (g) with a fixed frequency of 150 kHz and (h) 787 nm laser (1.3, 3.3, and 5.1 W/cm^2) in the dual-mode (9 kA/m, 150 kHz). (i) Optical image of pork tissue used for *ex vivo* dual-modal heating and their thermal images at 3 min post-injection of SASNs (II-BW) under three types of modulations (laser at 3.3 W/cm^2, AMF at 7 kA/m, and dual-mode). The injection point of the SASNs (II-BW) is denoted by a red circle. The blue circle indicates a location free of SASNs (II-BW) (non-injection spot), and the laser was focused on that spot without AMF in the control experiment.

the biological medium, and further, avoids their leakage to the exterior of the SASNs (II-BW). The biocompatibility of PVP has been proven to enhance the application of numerous PVP-capped NPs in the biomedical field.[52−54]

Understanding the biodistribution and clearance of SASNs (II-BW) is directly related to the safety issue and is of great importance for the biomedical application of SASNs *in vivo*. By collecting blood samples at desired time points from 0.5 to 24 h and measuring the Fe concentration in blood (Figure S9a), the blood circulation half-life of the SASNs (II-BW) in a mouse model was calculated to be 1.7 h. The relatively long blood circulation half-life is suitable for the effective accumulation of SASNs (II-BW) in the tumor site by the enhanced permeability and retention (EPR) effect.[55] In the meantime, the biodistribution of the SASNs (II-BW) in different organs of mice shows that the accumulation of SASNs (II-BW) in the liver and spleen becomes dominant at 24 h post-injection, as shown in Figure S9b. This observation of clearance of SASNs (II-BW) is similar to some previously reported studies, suggesting that the SASNs are mainly excreted through the reticuloendothelial system.[56,57]

To pursue high-performance MR imaging contrast agents, *i.e.*, high T_2 contrast relaxivity (r_2), many efforts have been undertaken to rationally engineer magnetic NPs by tuning their composition, size, shape, crystal structure, and surface properties.[58−66] In addition to the above strategies, another intriguing design is to form clusters of magnetic NPs from single magnetic NPs, which can lead to an obvious decrease of the T_2 relaxation time and thus an increase of the r_2 value. The reason for the enhanced relaxivity within NP clusters may be the cluster-induced increase of magnetic field inhomogeneity, which largely enhances the perturbation of proton phase coherence when water molecules diffuse around adjacent magnetic NPs.[38,67] Given a large number of Fe_3O_4 NPs in each SASN (II-BW), combined with their excellent superparamagnetic properties, SASNs (II-BW) were expected to be an ideal T_2 contrast agent with high relaxivity for MR imaging. To evaluate the T_2 MR imaging performance of SASNs (II-BW), the T_2-weighted MR images of various Fe concentrations of SASNs (II-BW) were acquired by a 3T clinical MR scanner, as shown in Figure 4a. At the same time, the free Fe_3O_4 NPs were also examined as a control (Figure 4a). Both SASNs (II-BW)

DOI: 10.1021/acsnano.8b06563
ACS Nano 2019, 13, 408−420

and free Fe_3O_4 NPs exhibit a concentration-dependent darkening effect of the negative T_2 MR contrast agent. However, the darkening effect of SASNs (II-BW) is significantly more pronounced than that of free Fe_3O_4 NPs. The relaxivity (r_2) of the SASNs (II-BW) was calculated to be approximately 282 mM^{-1} s^{-1}, which is more than ~3.7 times that of free Fe_3O_4 NPs (77 mM^{-1} s^{-1}) (Figure 4b), as well as several types of clinically approved Fe-based contrast agents (72 mM^{-1} s^{-1} for Ferumoxsil, 98.3 mM^{-1} s^{-1} for Ferumoxide, and 150 mM^{-1} s^{-1} for Resovist).[68] Such high relaxivity for the SASNs (II-BW) can be attributed to the synergistic MR enhancement effect of multiple Fe_3O_4 NPs aggregated inside the SASNs (II-BW), which is in agreement with previous reports.[38,67] This result strongly suggests the potential of SASNs (II-BW) as T_2 contrast agents for *in vivo* MR imaging, which was further explored. SASNs (II-BW) (200 μL, 2 mg/mL, dose = 10 mg/kg) were administered to a mouse bearing 4T1 tumors intravenously and imaged by a 3T clinical MR scanner. A noticeable darkening effect in the tumor area can be observed 12 h after post-injection (red dashed circles in Figure 4c), and the corresponding signal-to-noise ratio (SNR) value of the tumor region (Figure 4d) decreases significantly, which indicated passive accumulation of the SASNs (II-BW) in the tumors. Therefore, this remarkable T_2 negative effect makes the SASNs (II-BW) ideal as T_2 contrast agents for *in vivo* MR imaging. All together, these results suggest that SASNs (II-BW) possess excellent superparamagnetic properties, which renders them suitable for MR imaging and magnetic-driven applications.

In order to study the combined magnetothermal and photothermal capabilities of the SASNs (II-BW), we designed an experimental setup in which an Eppendorf tube containing a solution of SASNs (II-BW) was placed in the center of a magnetic coil and irradiated by a 787 nm laser (787 nm is an equally convenient excitation wavelength for bioimaging, located within the I-BW), and the temperature increase was recorded by a thermocouple, as shown in Figure 5a. By switching the laser and AMF on and off, we can realize three types of heating: photothermal (only by laser, at power densities of 1.3−5.1 W/cm^2), magnetothermal (only by AMF with a fixed frequency of 150 kHz and magnetic field amplitude from 3 to 9 kA/m), and combined magnetothermal and photothermal (dual-mode, simultaneously with the laser and AMF). Time-dependent temperature curves of SASNs (II-BW) solution at concentrations of 10 and 20 mM under 5 min of each modulation (laser at 3.3 W/cm^2, AMF at 7 kA/m, and dual-mode) were recorded and are presented in Figure 5b. The temperature of the two samples under three heating modalities increases monotonically with time, while the rate of temperature increase varies with different modalities (dual-mode > AMF > laser). We found that the temperature increase after 5 min of dual-mode heating (31 and 43 °C at 10 and 20 mM, respectively) is approximately equal to the sum of magnetothermal heating (22 and 31 °C for 10 and 20 mM samples under AMF, respectively) and photothermal heating (9 and 13 °C for 10 and 20 mM under laser irradiation, respectively). It is worth noting that differences in absolute temperatures and increase rates, when either of the heating modalities is used alone, stem from the fact that during the AMF modulation the SASNs (II-BW) solution is being heated homogeneously throughout the whole volume, whereas heating by laser irradiation is highly localized to the incident beam spot. Figure 5c shows the corresponding thermal images of SASNs (II-BW) solutions of 10 and 20 mM after 5 min of magnetic or optical modulation. It can be seen that dual-mode heating surpasses either photothermal or magnetothermal heating alone, while the magnetothermal heating is dominant in the dual-mode heating at the present experimental conditions. The temperature increase at different concentrations of SASNs (II-BW) after 5 min of each modulation (laser, AMF, and dual-mode) was investigated and is presented in Figure 5d, e, and f, respectively. Remarkably, the temperature increase of all the samples under dual-mode heating matches with the sum of the heating for laser or AMF conditions alone, which confirms the cumulative effect of dual-mode heating. It is important to note that pure water as a control shows only a very low temperature increase under laser irradiation and near zero increase under AMF. Hence, our technique can help to avoid damage to the surrounding biological tissues, which are in the absence of dual-mode thermal agents, during the treatments. We also compared PbS/CdS QDs and Fe_3O_4 NPs alone with the same concentration of SASNs (II-BW) under the three heating modalities (Figure S10). Of all the samples, SASNs (II-BW) exhibit much more promising heating capabilities than PbS/CdS QDs or Fe_3O_4 NPs individually, especially when dual-mode heating is considered.

The heat output of both photothermal and magnetothermal modalities can be tuned by varying the laser power density and the magnetic field (frequency and amplitude), respectively (Figures S11, S12). The efficiency of magnetothermal heating is usually expressed as SLP, and the values under AMF are plotted in Figure 5g. It can be seen that the SLP values increase with the increasing amplitude of the applied magnetic field. Moreover, photothermal heating increases with the laser's power density, expressed in W/cm^2, as shown in Figure S12. After combining laser irradiation with AMF (dual-mode) (Figure 5h), the SLP value surged up to 1883 W/g at a laser power density of 5.1 W/cm^2, which is almost 7 times higher than that of the maximum value under AMF (271 W/g). This result indicated that the SLP value was strongly enhanced by combining the laser irradiation. Although this value seems not very high, it can be easily understood since the magnetic field used in our work is several orders of magnitude lower than for the other reported studies in terms of frequency (150 kHz) and amplitude (from 3 to 9 kA/m) (Table S1). The conclusion was further supported by using a commercial ferrofluid (fluidMAG-PMO) solution as a control sample under dual-mode modulation (Figure S13, Table S1) and by comparing data obtained herein with their previously reported data. Given the SLP value of commercial ferrofluids is only one-third that of SASNs (II-BW), we believe that SASNs (II-BW) possess excellent heating capability with an excellent SLP value if comparable AMF was employed in combination with photothermal heating. Furthermore, we sought to evaluate the potential application of SASNs (II-BW) for dual-mode heating treatments in biological systems by *ex vivo* experiments. Briefly, a pork tissue sample was injected at *ca.* 2 mm in depth with 100 μL of an aqueous solution of SASNs (II-BW) (2 mg/mL). The pork tissue was then subjected to laser irradiation, AMF, and dual-mode, respectively, and the thermal images in each case were collected in order to determine the temperature increase at the surface of the tissue, as shown in Figure 5i. The average temperature at the injection site increased to 27 °C under the laser irradiation, while the temperature also slightly increased to 18 °C at the non-injection laser irradiated site in the control experiment (the initial temperature of pork tissue

DOI: 10.1021/acsnano.8b06563
ACS Nano 2019, 13, 408−420

was 17 °C), which indicates that significant heating occurs only at the injection site. In addition, it should be noted that the laser spot of 3.3 W/cm^2 power density, used in this experiment, did not cause any tissue damage (at the non-injection site) after irradiation for several minutes. The power density is comparable to that used in *in vivo* photothermal therapy based on gold nanorods and carbon nanotubes.[69,70] The temperature under AMF and dual-mode modulation increased to 38 and 45 °C after 3 min, respectively, and the temperature increase in the dual-mode manipulation exhibited the cumulative effect of individual modalities. At this point, we should note that the AMF for magnetothermal therapy *in vivo* is subject to a strict limitation of magnetic field frequency (f) and amplitude (H): $H \times f < 5 \times 10^9$ Am^{-1} s^{-1}, so as to avoid Eddy currents, which have been shown to induce non-selective heating and cardiac stimulation.[71] In our work, the fixed frequency (150 kHz) and magnetic field amplitude from 3 to 9 kA/m were within this safe application range. Therefore, notable *ex vivo* results suggest that SASNs (II-BW) could be potentially used as highly efficient nanoheaters for *in vivo* combined dual-mode thermal treatment.

CONCLUSIONS

In summary, multifunctional (superparamagnetic and NIR photoluminescent) SASNs (II-BW) were prepared by the self-assembly method, and their formation mechanism during the self-assembling process was studied. Under excitation with an 806 nm laser (I-BW), the SASNs (II-BW) allowed us to obtain NIR photoluminescence imaging with enhanced tissue penetration depth compared to that of SASNs (I-BW) due to minimized light extinction in biological tissues. In addition to their excellent NIR photoluminescence, the SASNs (II-BW) exhibit remarkable superparamagnetism, impressive photostability, and colloidal stability. Moreover, the MR imaging results indicate that SASNs (II-BW) can be used as promising T_2 contrast agents for *in vivo* MR imaging due to the significantly enhanced T_2 relaxivity arising from the clustered Fe_3O_4 NPs. The dual-mode heating studies with SASNs (II-BW) as heating agents showed an extremely efficient heating output at the local site. Overall this work opens a new avenue toward the use of SASNs (II-BW) for multifunctional theranostic applications, specifically, as NIR-excited deep-tissue bimodal imaging and dual-mode heating agents.

MATERIALS AND METHODS

Materials. Iron chloride hexahydrate ($FeCl_3 \cdot 6H_2O$), sodium oleate, oleic acid (OA, technical grade 90%), 1-octadecene (ODE, technical grade 90%), lead chloride ($PbCl_2$, 98%), lead acetate trihydrate ($Pb(OAc)_2 \cdot 3H_2O$, 99.9%), sulfur (S, 100%), bis(trimethylsilyl) sulfide ($(TMS)_2S$, synthesis grade), trioctylphosphine (TOP, 90%), oleylamine (OLA, technical grade, 70%), cadmium oxide (CdO, 99%), dimethyl sulfoxide (DMSO, ≥99.9%), polyvinylpyrrolidone (PVP, MW ~55 000), ethylene glycol (EG, 99.8%), and dodecyltrimethylammonium bromide (DTAB, 99%) were purchased from Sigma-Aldrich Inc. Commercial ferrofluids (fluidMAG-PMO, 25 mg/mL) with a size of 20 nm were purchased from Chemicell GmbH (Berlin, Germany). Hexane, toluene, methanol, and ethanol were purchased from Fisher Scientific Company. All chemicals were used as purchased.

Synthesis of Fe_3O_4 Magnetic Nanoparticles. The Fe_3O_4 NPs were synthesized by thermal decomposition of iron oleate precursor according to a previous report.[72] Typically, the iron oleate complex was prepared by refluxing of $FeCl_3 \cdot 6H_2O$ (1.08 g, 4 mmol) and sodium oleate (4.87 g, 16 mmol) in a mixture solution of ethanol (8 mL), distilled water (6 mL), and hexane (14 mL) at 70 °C for 6 h. After that, the iron oleate precursor was washed several times with hot distilled water in a separation funnel. The iron oleate precursor (0.9 g, 1 mmol) was then dissolved in a mixture of OA (142 mg, 0.5 mmol) and ODE (10 mL) and heated to 320 °C with the protection of N_2 for 1 h. The black Fe_3O_4 NPs were precipitated by centrifugation and washed with ethanol and hexane. The unreacted precursors were completely removed by repeating the centrifugation and washing several times. Finally, the Fe_3O_4 NPs were dispersed in chloroform as stock solution.

Synthesis of Smaller PbS (I-BW) QDs (Size: ~2.9 nm in Diameter). Smaller PbS (I-BW) QDs were synthesized by a hot-injection method.[73,74] Typically, $Pb(OAc)_2 \cdot 3H_2O$ (760 mg), OA (2.4 mL), and ODE (15 mL) were added into a three-neck flask and heated to 150 °C for 1 h with stirring and N_2 flow. Then the mixture was cooled to 130 °C under vacuum for 30 min. Subsequently, a 2 mL mixture of $(TMS)_2S$ and TOP (1:10 ratio by volume) was quickly injected into the flask, and the temperature was kept at 100 °C for 5 min under N_2 flow. Finally, the reaction was quenched by cold water. The PbS (I-BW) QDs dispersed in hexane were stored at 4 °C for 2 days, then centrifuged at 8000 rpm for 30 min to remove the sediment. Following the addition of methanol, the QDs were precipitated and redispersed in toluene. This purification was repeated one more time, and finally the QDs were dispersed in toluene for the growth of the CdS shell.

Synthesis of Larger PbS (II-BW) QDs (Size: ~4.7 nm in Diameter). Larger PbS (II-BW) QDs were synthesized by using OLA as capping ligands instead of OA for smaller PbS (I-BW) QDs.[40] Briefly, $PbCl_2$ (10 g) and OLA (24 mL) in a 50 mL flask were heated to 160 °C and degassed under vacuum for 1 h. The N_2 flow was then opened, and the $PbCl_2$−OLA solution was cooled to 120 °C. After that, sulfur (115 mg) in OLA (4 mL) was quickly injected into the above $PbCl_2$−OLA solution. The growth reaction of PbS QDs was kept at 100 °C for several minutes. When the PbS (II-BW) QDs reached the desired size, the reaction was quenched by cold water. The PbS (II-BW) QDs were purified by adding ethanol and toluene, followed by centrifugation to separate the PbS (II-BW) QDs. Last, the PbS (II-BW) QDs were dispersed in toluene for the further growth of the CdS shell.

Synthesis of Core/Shell PbS/CdS (I-BW and II-BW) QDs. PbS/CdS (I-BW) and PbS/CdS (II-BW) QDs were synthesized by a microwave-assisted cation exchange method.[40] In a typical reaction, CdO (3 g), OA (15 mL), and ODE (20 mL) were heated to 200 °C to form a colorless solution. The Cd oleate solution was then cooled to 100 °C and degassed under vacuum for 30 min. After this step, 8 mL of Cd oleate solution and 12 mL of PbS (I-BW)/PbS (II-BW) QDs in toluene were introduced into a 35 mL microwave reaction tube and heated to 100 °C under microwave radiation for several minutes. Finally, PbS/CdS QDs were purified by ethanol−toluene several times and dispersed in chloroform.

Synthesis of Self-Assembled Fe_3O_4 and PbS/CdS (II-BW) Supernanoparticles [SASNs (II-BW)] and Self-Assembled Fe_3O_4 and PbS/CdS (I-BW) Supernanoparticles [SASNs (I-BW)]. For a typical synthesis of SASNs (II-BW), 1 mL of Fe_3O_4 (4 mg) NPs and 1 mL of PbS/CdS (II-BW) QDs (6 mg) chloroform solution (molar ratio of Fe/Pb = 1:1.2) were injected into 1 mL of DTAB (20 mg/mL) aqueous solution. The solution was thoroughly mixed by vortex, following chloroform evaporation under N_2 flow. After that, the aqueous mixture of PbS/CdS (II-BW) QDs and Fe_3O_4 NPs was swiftly injected into a PVP-in-EG solution (20 mg/mL) and left under vigorous stirring for 4 h. The resulting SASNs (II-BW) were isolated by centrifugation, washed with ethanol, and finally dispersed in water.

SASNs (I-BW) were synthesized following the same procedure as the SASNs (II-BW), except for replacing PbS/CdS (II-BW) QDs (6 mg) with PbS/CdS (I-BW) QDs (6 mg).

Characterization. The crystal structure of all the samples was characterized by using a Bruker D8 ADVANCE X-ray diffractometer, equipped with a Cu anode X-ray source (Cu Kα, λ = 1.540 598 Å). The TEM images, HAADF-STEM images, and EDX-elemental

DOI: 10.1021/acsnano.8b06563
ACS Nano 2019, 13, 408−420

mapping were obtained using a JEOL 2100F microscope at 200 kV equipped with a charge-coupled device camera. The hydrodynamic size of the SASNs (II-BW) was characterized by a Malvern Zetasizer Nano-S90 DLS instrument. Content of Pb and Fe elements in the SASNs (II-BW) was assessed by ICP-OES (Agilent Technologies, 5100). FTIR spectra were collected in the range of 4000−500 cm^{-1} by using a ThermoFisher Scientific Nicolet 6700 FTIR spectrometer. The magnetic hysteresis loop was measured by a vibrating sample magnetometer (VSM, model 4 HF-VSM, ADE USA) at 300 K with a magnetic field up to 3 T. Temperature-dependent ZFC and FC magnetization curves were taken under an applied field of 100 Oe between 5 and 300 K. Absorption spectra of all the samples were measured by a UV−visible−NIR spectrophotometer (Cary 5000) with a scan speed of 600 nm/min. NIR photoluminescence spectra were acquired on a Fluorolog-3 system (Horiba Jobin Yvon) using an excitation wavelength of 600 nm.

Photoluminescence Time Trace Measurements for a Singled-out Aggregate of SASNs (II-BW). The NIR photoluminescence image of SASNs (II-BW) on a glass coverslip was taken using a multiphoton/NIR hyperspectral microscope (Photon Etc., Canada) with detection limits from 400 to 1750 nm, equipped with a pulsed femtosecond Ti:Sapphire Mai Tai laser as excitation source (Spectra Physics, USA) and an excitation wavelength fixed at 808 nm. The platform is based on the inverted epifluorescent microscope body (Nikon Eclipse Ti-S, Japan), equipped with a 20× 0.40 NA objective (Nikon, Japan). The collected photoluminescence signal is spectrally separated from the excitation beam by utilizing an appropriate NIR filter cube and passed onto the dispersive element from which the spectral information at a single excitation spot is registered with an InGaAs camera (Nunavut, BaySpec, USA). The fluorescence intensity trace was obtained from the NIR spectra of SASNs (II-BW) measurement every 52 s.

Cell Culture and Viability Assay. HeLa cervical cancer cells and human embryonic kidney (HEK 293T) cells were cultured in Dulbecco's modified Eagle's medium (DMEM), 10% fetal bovine serum (FBS), 50 units/mL penicillin, and 50 units/mL streptomycin in 5% CO_2 at 37 °C. HEK 293T and HeLa cells were plated at 5×10^5 cells/well into a 96-well plate and incubated for 24 h in DMEM (100 μL). Cells were then treated with SASNs (II-BW) at various concentration. Blank controls without SASNs (II-BW) (cells only) were run simultaneously. Cell viability was measured by using a CellTiter 96 Non-Radioactive cell proliferation assay kit (MTT, Promega) according to the manufacturer's protocol. Briefly, 3-(4,5-dimethylthiazol-2-yl)-2,5-diphenyltetrazolium bromide (MTT) solutions (15 μL) were added into each well. The medium containing unreacted MTT was carefully removed after 24 h of incubation. Then DMSO (100 μL) was added into each well in order to dissolve the formed formazan blue crystals, and the absorbance at $\lambda = 570$ nm was recorded using a Powerwave HT microplate reader (Bio-Tek). Each concentration was 6-replicated ($n = 6$). Cell viability was calculated as the percent ratio of mixtures with SASNs (II-BW) to control (cells only).

NIR Imaging *ex Vivo*. NIR images were taken by an Xeva-1.7 infrared camera (Xenics Corp) equipped with a 830 nm filter to record images in the specific spectral range and to block the scattered excitation light. The 806 nm laser diode was used as a fixed excitation source ((Lumics, power density of 10 W/cm^2).

Animal Model. 4T1 murine breast cancer cells were cultured in standard cell media recommended by American Type Culture Collection (ATCC). Female Balb/c mice were purchased from Nanjing Peng Sheng Biological Technology Co. Ltd. and used under protocols approved by Soochow University Laboratory Animal Center.

T_2 Relaxivity Measurements *in Vitro* and MR Imaging *in Vivo*. T_2-weighted MR images were acquired by a 3T clinic MRI scanner (Bruker Biospin Corporation, Billerica, MA, USA) at room temperature. SASNs (II-BW) in PBS buffer with different concentrations were placed in a series of tubes for T_2-weighted MR imaging. The concentration of Fe was determined by ICP-OES (Agilent Technologies, 5100). The relaxivity value (r_2) was calculated based on the fitting curve of $1/T_2$ relaxation time (s^{-1}) *vs* the concentration of Fe (mM).

A mouse bearing one 4T1 tumor was administered with SASNs (II-BW) in PBS buffer (200 μL, 2 mg/mL, dose = 10 mg/kg) by an intravenous injection *via* its tail vein. The MR imaging of the mouse was conducted on the same scanner equipped with a special coil designed for small animal imaging. The mouse was scanned before and after injection of the contrast agent.

Biodistribution Study. SASNs (II-BW) in PBS buffer (200 μL, 2 mg/mL, dose = 10 mg/kg) were injected into the mice intravenously. Blood samples were collected from the facial vein at the desired time points (30 min and 1, 2, 4, 6, 12, and 24 h). The Fe content in blood was determined by ICP-OES after the red blood cells were removed by centrifugation. The following organs including liver, heart, spleen, kidneys, and lungs were collected, weighed, completely lysed in aqua regia, and examined by ICP-OES at 24 h post-injection. The biodistribution results were expressed as the percentage of injected dose per gram of organ (% ID/g)

Photothermal, Magnetic Hyperthermia and Dual-Mode Measurements *in Vitro*. For magnetic hyperthermia experiment, the alternating magnetic field was generated by a magnetothermal equipment (Ameritherm Inc., New York), consisting of a coil (3 turns of loops of Cu pipe, 6 cm in diameter), which was cooled by a water circulation system. The magnetic field frequency was fixed at 150 kHz, and the magnetic field amplitude could be tuned by the current from 0 to 180 A. Magnetic field amplitude (H) was calculated by the equation

$$H = n\frac{\mu_0 I}{2R}$$

where $\mu_0 = 4\pi \times 10^{-7}$ T·m/A, n is the number of turns, R is the loop radius, and I is the applied current.

Typically, a solution (0.6 mL) of SASNs (II-BW) in an Eppendorf tube, surrounded by Styrofoam to minimize possible external temperature fluctuations, was placed at the center of the coil, and the temperature increase was recorded by a computer-attached optical fiber based thermocouple (Reflex, SN:T18 217A, Neoptix Inc., Canada).

For laser photothermal experiments, a continuous wave portable 787 nm NIR laser (Ningbo Lasever Inc., China) was used as an irradiation source. An Eppendorf tube containing the SASNs (II-BW) solution was irradiated by the laser placed on the same holder at the center of coil as for the magnetic hyperthermia experiment (the magnetic field was switched off). The distance between laser and sample was fixed at 13 cm. The temperature increase was recorded by the same sensor above.

For the dual-mode heating experiment, the same configuration for laser photothermal experiment was adopted while keeping the magnetic field on.

Thermal images were recorded by an infrared thermal imaging camera (FLIR E4, FLIR Systems AB, Sweden) from the top of the sample.

Specific loss power is defined as the power dissipation per unit mass of magnetic material (W/g) in order to evaluate the heating effect. The SLP values of different samples were calculated based on the following equation:

$$\mathrm{SLP} = C\frac{\Delta T V}{\Delta t m}$$

where C is the specific heat capacity of the medium (C_{water} = 4185 J/L/K), $\Delta T/\Delta t$ is the initial slope of the time-dependent temperature curve ($t \approx 30$ s), V is the volume of the sample, and m is the total mass of magnetic material in the sample.[75]

A discussion regarding the use of three different wavelength NIR lasers (787, 806, 808 nm) and the excitation spectrum of SASNs (II-BW) are provided in Figure S14 to avoid confusion and to clarify that the difference in these wavelengths does not have any significant effect on relevant experiments.

DOI: 10.1021/acsnano.8b06563
ACS Nano 2019, 13, 408−420

ASSOCIATED CONTENT

Supporting Information

The Supporting Information is available free of charge on the ACS Publications website at DOI: 10.1021/acsnano.8b06563.

Additional explanations about data and Figures S1−S14 (PDF)

AUTHOR INFORMATION

Corresponding Authors

*E-mail: vetrone@emt.inrs.ca.

*E-mail: ma@emt.inrs.ca.

ORCID

Fan Yang: 0000-0001-6306-4501

Artiom Skripka: 0000-0003-4060-4290

Jung Kwon Oh: 0000-0002-4220-308X

Fiorenzo Vetrone: 0000-0002-3222-3052

Dongling Ma: 0000-0001-8558-3150

Notes

The authors declare no competing financial interest.

ACKNOWLEDGMENTS

D.M. and F.V. are grateful to the Natural Sciences and Engineering Research Council of Canada (NSERC: RGPIN-2015-06756) and the Fonds de Recherche du Québec−Nature et Technologies (FRQNT: 2014-PR-174462) for funding. F.Y., F.R., and A.S. greatly appreciate the financial support from the Merit Scholarship Program for Foreign Students from the Ministère de l'Éducation, du Loisir et du Sport du Québec (No. 193353, No. 255072, and No. 257149). We would like to thank J.X. from Soochow University for the help with *in vivo* experiments. We acknowledge Z.Y. from Peking University for the magnetic characterization.

REFERENCES

(1) Yang, F.; Skripka, A.; Benayas, A.; Dong, X.; Hong, S. H.; Ren, F.; Oh, J. K.; Liu, X.; Vetrone, F.; Ma, D. An Integrated Multifunctional Nanoplatform for Deep-Tissue Dual-Mode Imaging. *Adv. Funct. Mater.* **2018**, *28*, 1706235.

(2) Kim, J.; Lee, J. E.; Lee, S. H.; Yu, J. H.; Lee, J. H.; Park, T. G.; Hyeon, T. Designed Fabrication of a Multifunctional Polymer Nanomedical Platform for Simultaneous Cancer- Targeted Imaging and Magnetically Guided Drug Delivery. *Adv. Mater.* **2008**, *20*, 478−483.

(3) Corr, S. A.; Rakovich, Y. P.; Gun'ko, Y. K. Multifunctional Magnetic-Fluorescent Nanocomposites for Biomedical Applications. *Nanoscale Res. Lett.* **2008**, *3*, 87.

(4) Xia, A.; Gao, Y.; Zhou, J.; Li, C.; Yang, T.; Wu, D.; Wu, L.; Li, F. Core-Shell $NaYF_4$:Yb^{3+},Tm^{3+}@Fe_xO_y Nanocrystals for Dual-Modality T_2-Enhanced Magnetic Resonance and NIR-to-NIR Upconversion Luminescent Imaging of Small-Animal Lymphatic Node. *Biomaterials* **2011**, *32*, 7200−7208.

(5) Villa, I.; Vedda, A.; Cantarelli, I. X.; Pedroni, M.; Piccinelli, F.; Bettinelli, M.; Speghini, A.; Quintanilla, M.; Vetrone, F.; Rocha, U.; Jacinto, C.; Carrasco, E.; Rodríguez, F. S.; Juarranz, Á.; Rosal, B.; Ortgies, D. H.; Gonzalez, P. H.; Solé, J. G.; García, D. J. 1.3 μm Emitting SrF_2:Nd^{3+} Nanoparticles for High Contrast *In Vivo* Imaging in the Second Biological Window. *Nano Res.* **2015**, *8*, 649−665.

(6) Hemmer, E.; Benayas, A.; Legare, F.; Vetrone, F. Exploiting the Biological Windows: Current Perspectives on Fluorescent Bioprobes Emitting above 1000 nm. *Nanoscale Horiz.* **2016**, *1*, 168−184.

(7) Vijayaraghavan, P.; Liu, C. H.; Vankayala, R.; Chiang, C. S.; Hwang, K. C. Designing Multi-Branched Gold Nanoechinus for NIR Light Activated Dual Modal Photodynamic and Photothermal Therapy in the Second Biological Window. *Adv. Mater.* **2014**, *26*, 6689−6695.

(8) Jiang, Y.; Pu, K. Multimodal Biophotonics of Semiconducting Polymer Nanoparticles. *Acc. Chem. Res.* **2018**, *51*, 1840−1849.

(9) Chinen, A. B.; Guan, C. M.; Ferrer, J. R.; Barnaby, S. N.; Merkel, T. J.; Mirkin, C. A. Nanoparticle Probes for the Detection of Cancer Biomarkers, Cells, and Tissues by Fluorescence. *Chem. Rev.* **2015**, *115*, 10530−10574.

(10) Miao, Q.; Pu, K. Organic Semiconducting Agents for Deep-Tissue Molecular Imaging: Second Near-Infrared Fluorescence, Self-Luminescence, and Photoacoustics. *Adv. Mater.* **2018**, *30*, 1801778.

(11) Jiang, Y.; Li, J.; Zhen, X.; Xie, C.; Pu, K. Dual-Peak Absorbing Semiconducting Copolymer Nanoparticles for First and Second Near-Infrared Window Photothermal Therapy: A Comparative Study. *Adv. Mater.* **2018**, *30*, 1705980.

(12) Zhang, M.; Yue, J.; Cui, R.; Ma, Z.; Wan, H.; Wang, F.; Zhu, S.; Zhou, Y.; Kuang, Y.; Zhong, Y.; Pang, D.; Dai, H. Bright Quantum Dots Emitting at ∼ 1,600 nm in the NIR-IIb Window for Deep Tissue Fluorescence Imaging. *Proc. Natl. Acad. Sci. U. S. A.* **2018**, *115*, 6590.

(13) Ma, Z.; Zhang, M.; Yue, J.; Alcazar, C.; Zhong, Y.; Doyle, T. C.; Dai, H.; Huang, N. F. Near-Infrared IIb Fluorescence Imaging of Vascular Regeneration with Dynamic Tissue Perfusion Measurement and High Spatial Resolution. *Adv. Funct. Mater.* **2018**, *28*, 1803417.

(14) Zhao, H.; Chaker, M.; Ma, D. Bimodal Photoluminescence During the Growth of PbS Quantum Dots. *J. Phys. Chem. C* **2009**, *113*, 6497−6504.

(15) Zhao, H.; Wang, D.; Zhang, T.; Chaker, M.; Ma, D. Two-Step Synthesis of High-Quality Water-Soluble Near-Infrared Emitting Quantum Dots *via* Amphiphilic Polymers. *Chem. Commun.* **2010**, *46*, 5301−3.

(16) Zhao, H.; Chaker, M.; Wu, N.; Ma, D. Towards Controlled Synthesis and Better Understanding of Highly Luminescent PbS/CdS Core/Shell Quantum Dots. *J. Mater. Chem.* **2011**, *21*, 8898−8904.

(17) Benayas, A.; Ren, F.; Carrasco, E.; Marzal, V.; Rosal, B.; Gonfa, B. A.; Juarranz, Á.; Sanz-Rodríguez, F.; Jaque, D.; García-Solé, J.; Ma, D.; Vetrone, F. PbS/CdS/ZnS Quantum Dots: A Multifunctional Platform for *In Vivo* Near-Infrared Low-Dose Fluorescence Imaging. *Adv. Funct. Mater.* **2015**, *25*, 6650−6659.

(18) Ren, F.; Rosal, B.; An, S. Y.; Yang, F.; Carrasco, E.; Benayas, A.; Oh, J. K.; Jaque, D.; de la Fuente, Á. J.; Vetrone, F. Development and Investigation of Ultrastable PbS/CdS/ZnS Quantum Dots for Near-Infrared Tumor Imaging. *Part. Part. Syst. Charact.* **2017**, *34*, 1600242.

(19) Tan, L.; Zhou, Y.; Ren, F.; Benetti, D.; Yang, F.; Zhao, H.; Rosei, F.; Chaker, M.; Ma, D. Ultrasmall PbS Quantum Dots: A Facile and Greener Synthetic Route and Their High Performance in Luminescent Solar Concentrators. *J. Mater. Chem. A* **2017**, *5*, 10250−10260.

(20) Ren, F.; Lindley, S. A.; Zhao, H.; Tan, L.; Gonfa, B. A.; Pu, Y. C.; Yang, F.; Liu, X.; Vidal, F.; Zhang, J. Z.; Vetrone, F.; Ma, D. Towards Understanding the Unusual Photoluminescence Intensity Variation of Ultrasmall Colloidal PbS Quantum Dots with the Formation of a Thin CdS Shell. *Phys. Chem. Chem. Phys.* **2016**, *18*, 31828−31835.

(21) Tan, L.; Yang, F.; Kim, M. R.; Li, P.; Gangadharan, D. T.; Margot, J.; Izquierdo, R.; Chaker, M.; Ma, D. Enhanced Long-Term and Thermal Stability of Polymer Solar Cells in Air at High Humidity with the Formation of Unusual Quantum Dot Networks. *ACS Appl. Mater. Interfaces* **2017**, *9*, 26257−26267.

(22) Xu, Z.; Liu, Y.; Ren, F.; Yang, F.; Ma, D. Development of Functional Nanostructures and Their Applications in Catalysis and Solar Cells. *Coord. Chem. Rev.* **2016**, *320*, 153−180.

(23) Fortin, J. P.; Wilhelm, C.; Servais, J.; Ménager, C.; Bacri, J. C.; Gazeau, F. Size-Sorted Anionic Iron Oxide Nanomagnets as Colloidal Mediators for Magnetic Hyperthermia. *J. Am. Chem. Soc.* **2007**, *129*, 2628−2635.

(24) Johannsen, M.; Gneveckow, U.; Eckelt, L.; Feussner, A.; Waldöfner, N.; Scholz, R.; Deger, S.; Wust, P.; Loening, S.; Jordan, A. Clinical Hyperthermia of Prostate Cancer Using Magnetic Nano-

particles: Presentation of a New Interstitial Technique. *Int. J. Hyperthermia* **2005**, *21*, 637−647.
(25) Akiyama, S.; Kawasaki, S.; Kodera, Y.; Hibi, K.; Kato, S.; Ito, K.; Nakao, A. A New Method of Thermo-Chemotherapy Using a Stent for Patients with Esophageal Cancer. *Surg. Today* **2005**, *36*, 19−24.
(26) Maier-Hauff, K.; Ulrich, F.; Nestler, D.; Niehoff, H.; Wust, P.; Thiesen, B.; Orawa, H.; Budach, V.; Jordan, A. Efficacy and Safety of Intratumoral Thermotherapy Using Magnetic Iron-Oxide Nanoparticles Combined with External Beam Radiotherapy on Patients with Recurrent Glioblastoma Multiforme. *J. Neuro-Oncol.* **2011**, *103*, 317−324.
(27) MagForce AG. MagForce AG Corporate News. https://www.magforce.com/en/presse-investoren/news-events/corporate-news/corporate-news-archiv/browse/1/select_category/23.html (accessed Dec 28, 2018).
(28) Zou, L.; Wang, H.; He, B.; Zeng, L.; Tan, T.; Cao, H.; He, X.; Zhang, Z.; Guo, S.; Li, Y. Current Approaches of Photothermal Therapy in Treating Cancer Metastasis with Nanotherapeutics. *Theranostics* **2016**, *6*, 762.
(29) Li, J.; Zhen, X.; Lyu, Y.; Jiang, Y.; Huang, J.; Pu, K. Cell Membrane Coated Semiconducting Polymer Nanoparticles for Enhanced Multimodal Cancer Phototheranostics. *ACS Nano* **2018**, *12*, 8520−8530.
(30) Zhen, X.; Zhang, J.; Huang, J.; Xie, C.; Miao, Q.; Pu, K. Macrotheranostic Probe with Disease-Activated Near-Infrared Fluorescence, Photoacoustic, and Photothermal Signals for Imaging-Guided Therapy. *Angew. Chem., Int. Ed.* **2018**, *57*, 7804−7808.
(31) Lyu, Y.; Cui, D.; Sun, H.; Miao, Y.; Duan, H.; Pu, K. Dendronized Semiconducting Polymer as Photothermal Nanocarrier for Remote Activation of Gene Expression. *Angew. Chem.* **2017**, *129*, 9283−9287.
(32) Rosal, B.; Carrasco, E.; Ren, F.; Benayas, A.; Vetrone, F.; Sanz-Rodríguez, F.; Ma, D.; Juarranz, Á.; Jaque, D. Infrared-Emitting QDs for Thermal Therapy with Real-Time Subcutaneous Temperature Feedback. *Adv. Funct. Mater.* **2016**, *26*, 6060.
(33) Lee, J.-H.; Jang, J.-t.; Choi, J.-s.; Moon, S. H.; Noh, S.-h.; Kim, J.-w.; Kim, J.-G.; Kim, I.-S.; Park, K. I.; Cheon, J. Exchange-Coupled Magnetic Nanoparticles for Efficient Heat Induction. *Nat. Nanotechnol.* **2011**, *6*, 418−422.
(34) Johannsen, M.; Gneveckow, U.; Thiesen, B.; Taymoorian, K.; Cho, C. H.; Waldöfner, N.; Scholz, R.; Jordan, A.; Loening, S. A.; Wust, P. Thermotherapy of Prostate Cancer Using Magnetic Nanoparticles: Feasibility, Imaging, and Three-Dimensional Temperature Distribution. *Eur. Urol.* **2007**, *52*, 1653−1662.
(35) Espinosa, A.; Di Corato, R.; Kolosnjaj-Tabi, J.; Flaud, P.; Pellegrino, T.; Wilhelm, C. Duality of Iron Oxide Nanoparticles in Cancer Therapy: Amplification of Heating Efficiency by Magnetic Hyperthermia and Photothermal Bimodal Treatment. *ACS Nano* **2016**, *10*, 2436−2446.
(36) Wang, T.; LaMontagne, D.; Lynch, J.; Zhuang, J.; Cao, Y. C. Colloidal Superparticles from Nanoparticle Assembly. *Chem. Soc. Rev.* **2013**, *42*, 2804−2823.
(37) Chen, J.; Dong, A.; Cai, J.; Ye, X.; Kang, Y.; Kikkawa, J. M.; Murray, C. B. Collective Dipolar Interactions in Self-Assembled Magnetic Binary Nanocrystal Superlattice Membranes. *Nano Lett.* **2010**, *10*, 5103−5108.
(38) Zhou, Z.; Tian, R.; Wang, Z.; Yang, Z.; Liu, Y.; Liu, G.; Wang, R.; Gao, J.; Song, J.; Nie, L. Artificial Local Magnetic Field Inhomogeneity Enhances T_2 Relaxivity. *Nat. Commun.* **2017**, *8*, 15468.
(39) Chen, O.; Riedemann, L.; Etoc, F.; Herrmann, H.; Coppey, M.; Barch, M.; Farrar, C. T.; Zhao, J.; Bruns, O. T.; Wei, H.; Guo, P.; Cui, J.; Jensen, R.; Chen, Y.; Harris, D. K.; Cordero, J. M.; Wang, Z.; Jasanoff, A.; Fukumura, D.; Reimer, R.; Dahan, M.; Jain, R. K.; Bawendi, M. G. Magneto-Fluorescent Core-Shell Supernanoparticles. *Nat. Commun.* **2014**, *5*, 5093.
(40) Ren, F.; Zhao, H.; Vetrone, F.; Ma, D. Microwave-Assisted Cation Exchange Toward Synthesis of Near-Infrared Emitting PbS/CdS Core/Shell Quantum Dots with Significantly Improved Quantum Yields Through a Uniform Growth Path. *Nanoscale* **2013**, *5*, 7800.
(41) Zhuang, J.; Wu, H.; Yang, Y.; Cao, Y. C. Controlling Colloidal Superparticle Growth Through Solvophobic Interactions. *Angew. Chem., Int. Ed.* **2008**, *47*, 2208−2212.
(42) Zhuang, J.; Wu, H.; Yang, Y.; Cao, Y. C. Supercrystalline Colloidal Particles from Artificial Atoms. *J. Am. Chem. Soc.* **2007**, *129*, 14166−14167.
(43) Wang, D.; He, J.; Rosenzweig, N.; Rosenzweig, Z. Superparamagnetic Fe_2O_3 Beads-CdSe/ZnS Quantum Dots Core-Shell Nanocomposite Particles for Cell Separation. *Nano Lett.* **2004**, *4*, 409−413.
(44) Li, M.; You, G.; Wang, A. Y.; Hu, W.; Wang, J.; Sun, F.; Zhu, Y.; Henderson, R.; Xu, J. Lasing and Magnetic Microbeads Loaded with Colloidal Quantum Dots and Iron Oxide Nanocrystals. *Nanoscale* **2013**, *5*, 9598−9603.
(45) Jafari, D.; Cody, K.; Dean, A.; Shofer, F.; Jenq, K.; Fischer, J.; Panebianco, N. Human or Animal? Finding the Best Ultrasound Soft Tissue Model for Foreign Body Evaluation. *Crit Ultrasound J.* **2012**, *4*, A18.
(46) Wang, Y. F.; Liu, G. Y.; Sun, L. D.; Xiao, J. W.; Zhou, J. C.; Yan, C. H. Nd^{3+}-Sensitized Upconversion Nanophosphors: Efficient *In Vivo* Bioimaging Probes with Minimized Heating Effect. *ACS Nano* **2013**, *7*, 7200−7206.
(47) Skripka, A.; Marin, R.; Benayas, A.; Canton, P.; Hemmer, E.; Vetrone, F. Covering the Optical Spectrum Through Collective Rare-Earth Doping of $NaGdF_4$ Nanoparticles: 806 and 980 nm Excitation Routes. *Phys. Chem. Chem. Phys.* **2017**, *19*, 11825−11834.
(48) Liang, H.; Vu, K. T.; Krishnan, P.; Trang, T. C.; Shin, D.; Kimel, S.; Berns, M. W. Wavelength Dependence of Cell Cloning Efficiency After Optical Trapping. *Biophys. J.* **1996**, *70*, 1529−1533.
(49) Johnston, B. D.; Kreyling, W. G.; Pfeiffer, C.; Schäffler, M.; Sarioglu, H.; Ristig, S.; Hirn, S.; Haberl, N.; Thalhammer, S.; Hauck, S. M. Colloidal Stability and Surface Chemistry Are Key Factors for the Composition of the Protein Corona of Inorganic Gold Nanoparticles. *Adv. Funct. Mater.* **2017**, *27*, 1701956.
(50) Hansen, M. F.; Mørup, S. Estimation of Blocking Temperatures from ZFC/FC Curves. *J. Magn. Magn. Mater.* **1999**, *203*, 214−216.
(51) Cannas, C.; Casula, M. F.; Concas, G.; Corrias, A.; Gatteschi, D.; Falqui, A.; Musinu, A.; Sangregorio, C.; Spano, G. Magnetic Properties of γ-Fe_2O_3-SiO_2 Aerogel and Xerogel Nanocomposite Materials. *J. Mater. Chem.* **2001**, *11*, 3180−3187.
(52) Koczkur, K. M.; Mourdikoudis, S.; Polavarapu, L.; Skrabalak, S. E. Polyvinylpyrrolidone (PVP) in Nanoparticle Synthesis. *Dalton Trans.* **2015**, *44*, 17883−17905.
(53) Tang, F.; Li, L.; Chen, D. Mesoporous Silica Nanoparticles: Synthesis, Biocompatibility and Drug Delivery. *Adv. Mater.* **2012**, *24*, 1504−1534.
(54) Xiao, L.; Li, J.; Brougham, D. F.; Fox, E. K.; Feliu, N.; Bushmelev, A.; Schmidt, A.; Mertens, N.; Kiessling, F.; Valldor, M. Water-Soluble Superparamagnetic Magnetite Nanoparticles with Biocompatible Coating for Enhanced Magnetic Resonance Imaging. *ACS Nano* **2011**, *5*, 6315−6324.
(55) Matsumura, Y.; Maeda, H. A New Concept for Macromolecular Therapeutics in Cancer Chemotherapy: Mechanism of Tumoritropic Accumulation of Proteins and the Antitumor Agent Smancs. *Cancer Res.* **1986**, *46*, 6387−6392.
(56) Duan, X.; Li, Y. Physicochemical Characteristics of Nanoparticles Affect Circulation, Biodistribution, Cellular Internalization, and Trafficking. *Small* **2013**, *9*, 1521−1532.
(57) Wang, Z.; Qiao, R.; Tang, N.; Lu, Z.; Wang, H.; Zhang, Z.; Xue, X.; Huang, Z.; Zhang, S.; Zhang, G. Active Targeting Theranostic Iron Oxide Nanoparticles for MRI and Magnetic Resonance-Guided Focused Ultrasound Ablation of Lung Cancer. *Biomaterials* **2017**, *127*, 25−35.
(58) Jun, Y.-w.; Huh, Y.-M.; Choi, J.-s.; Lee, J.-H.; Song, H.-T.; Yoon, S.; Kim, K.-S.; Shin, J.-S; Suh, J.-S.; Cheon, J. Nanoscale Size Effect of Magnetic Nanocrystals and Their Utilization for Cancer

DOI: 10.1021/acsnano.8b06563
ACS Nano 2019, 13, 408−420

Diagnosis *via* Magnetic Resonance Imaging. *J. Am. Chem. Soc.* **2005**, *127*, 5732−5733.
(59) Tromsdorf, U. I.; Bigall, N. C.; Kaul, M. G.; Bruns, O. T.; Nikolic, M. S.; Mollwitz, B.; Sperling, R. A.; Reimer, R.; Hohenberg, H.; Parak, W. J. Size and Surface Effects on the MRI Relaxivity of Manganese Ferrite Nanoparticle Contrast Agents. *Nano Lett.* **2007**, *7*, 2422−2427.
(60) Zhao, Z.; Zhou, Z.; Bao, J.; Wang, Z.; Hu, J.; Chi, X.; Ni, K.; Wang, R.; Chen, X.; Chen, Z.; Gao, J. Octapod Iron Oxide Nanoparticles as High-Performance T_2 Contrast Agents for Magnetic Resonance Imaging. *Nat. Commun.* **2013**, *4*, 2266.
(61) Pöselt, E.; Kloust, H.; Tromsdorf, U.; Janschel, M.; Hahn, C.; Maßlo, C.; Weller, H. Relaxivity Optimization of a PEGylated Iron-Oxide-Based Negative Magnetic Resonance Contrast Agent for T_2-Weighted Spin-Echo Imaging. *ACS Nano* **2012**, *6*, 1619−1624.
(62) Zhou, Z.; Zhao, Z.; Zhang, H.; Wang, Z.; Chen, X.; Wang, R.; Chen, Z.; Gao, J. Interplay Between Longitudinal and Transverse Contrasts in Fe_3O_4 Nanoplates with (111) Exposed Surfaces. *ACS Nano* **2014**, *8*, 7976−7985.
(63) Jang, J.-t.; Nah, H.; Lee, J.-H.; Moon, S. H.; Kim, M. G.; Cheon, J. Critical Enhancements of MRI Contrast and Hyperthermic Effects by Dopant-Controlled Magnetic Nanoparticles. *Angew. Chem.* **2009**, *121*, 1260−1264.
(64) Yang, D.; Yang, G.; Yang, P.; Lv, R.; Gai, S.; Li, C.; He, F.; Lin, J. Assembly of Au Plasmonic Photothermal Agent and Iron Oxide Nanoparticles on Ultrathin Black Phosphorus for Targeted Photothermal and Photodynamic Cancer Therapy. *Adv. Funct. Mater.* **2017**, *27*, 1700371.
(65) Xu, J.; Han, W.; Yang, P.; Jia, T.; Dong, S.; Bi, H.; Gulzar, A.; Yang, D.; Gai, S.; He, F. Tumor Microenvironment-Responsive Mesoporous MnO_2-Coated Upconversion Nanoplatform for Self-Enhanced Tumor Theranostics. *Adv. Funct. Mater.* **2018**, *28*, 1803804.
(66) Xu, J.; He, F.; Cheng, Z.; Lv, R.; Dai, Y.; Gulzar, A.; Liu, B.; Bi, H.; Yang, D.; Gai, S. Yolk-Structured Upconversion Nanoparticles with Biodegradable Silica Shell for FRET Sensing of Drug Release and Imaging-Guided Chemotherapy. *Chem. Mater.* **2017**, *29*, 7615−7628.
(67) Paquet, C.; de Haan, H. W.; Leek, D. M.; Lin, H.-Y.; Xiang, B.; Tian, G.; Kell, A.; Simard, B. Clusters of Superparamagnetic Iron Oxide Nanoparticles Encapsulated in a Hydrogel: A Particle Architecture Generating a Synergistic Enhancement of the T_2 Relaxation. *ACS Nano* **2011**, *5*, 3104−3112.
(68) Zhao, H. X.; Zou, Q.; Sun, S. K.; Yu, C.; Zhang, X.; Li, R. J.; Fu, Y. Y. Theranostic Metal-Organic Framework Core-Shell Composites for Magnetic Resonance Imaging and Drug Delivery. *Chem. Sci.* **2016**, *7*, 5294−5301.
(69) Maestro, L. M.; Haro-González, P.; Rosal, B.; Ramiro, J.; Caamano, A.; Carrasco, E.; Juarranz, A.; Sanz-Rodríguez, F.; Solé, J. G.; Jaque, D. Heating Efficiency of Multi-Walled Carbon Nanotubes in the First and Second Biological Windows. *Nanoscale* **2013**, *5*, 7882−7889.
(70) Robinson, J. T.; Welsher, K.; Tabakman, S. M.; Sherlock, S. P.; Wang, H.; Luong, R.; Dai, H. High Performance *In Vivo* Near-IR (> 1 μm) Imaging and Photothermal Cancer Therapy with Carbon Nanotubes. *Nano Res.* **2010**, *3*, 779−793.
(71) Hergt, R.; Dutz, S. Magnetic Particle Hyperthermia-Biophysical Limitations of a Visionary Tumour Therapy. *J. Magn. Magn. Mater.* **2007**, *311*, 187−192.
(72) Park, J.; An, K.; Hwang, Y.; Park, J.-G.; Noh, H.-J.; Kim, J.-Y.; Park, J.-H.; Hwang, N.-M.; Hyeon, T. Ultra-Large-Scale Syntheses of Monodisperse Nanocrystals. *Nat. Mater.* **2004**, *3*, 891−5.
(73) Hines, M. A.; Scholes, G. D. Colloidal PbS Nanocrystals with Size-Tunable Near-Infrared Emission: Observation of Post-Synthesis Self-Narrowing of the Particle Size Distribution. *Adv. Mater.* **2003**, *15*, 1844−1849.
(74) Zhang, T.; Zhao, H.; Riabinina, D.; Chaker, M.; Ma, D. Concentration-Dependent Photoinduced Photoluminescence Enhancement in Colloidal PbS Quantum Dot Solution. *J. Phys. Chem. C* **2010**, *114*, 10153−10159.
(75) Soetaert, F.; Kandala, S. K.; Bakuzis, A.; Ivkov, R. Experimental Estimation and Analysis of Variance of the Measured Loss Power of Magnetic Nanoparticles. *Sci. Rep.* **2017**, *7*, 6661.

DOI: 10.1021/acsnano.8b06563
ACS Nano 2019, 13, 408−420